

# Gyro-fluid and two-fluid theory and simulations of edge-localized-modes<sup>a)</sup>

X. Q. Xu,<sup>1,b)</sup> P. W. Xi,<sup>1,2</sup> A. Dimits,<sup>1</sup> I. Joseph,<sup>1</sup> M. V. Umansky,<sup>1</sup> T. Y. Xia,<sup>1,3</sup> B. Gui,<sup>1,3</sup>  
 S. S. Kim,<sup>4</sup> G. Y. Park,<sup>4</sup> T. Rhee,<sup>4</sup> H. Jhang,<sup>4</sup> P. H. Diamond,<sup>4,5</sup> B. Dudson,<sup>6</sup>  
 and P. B. Snyder<sup>7</sup>

<sup>1</sup>Lawrence Livermore National Laboratory, Livermore, California 94551, USA

<sup>2</sup>School of Physics, Peking University, Beijing, China

<sup>3</sup>Institute of Plasma Physics, Chinese Academy of Sciences, Hefei, China

<sup>4</sup>WCI Center for Fusion Theory, National Fusion Research Institute, Daejeon 305-333, South Korea

<sup>5</sup>Center for Astrophysics and Space Sciences and Department of Physics, University of California, San Diego, La Jolla, California 92093-0424, USA

<sup>6</sup>University of York, Heslington, York YO10 5DD, United Kingdom

<sup>7</sup>General Atomics, San Diego, California 92186, USA

(Received 3 December 2012; accepted 29 January 2013; published online 17 May 2013)

This paper reports on the theoretical and simulation results of a gyro-Landau-fluid extension of the BOUT++ code, which contributes to increasing the physics understanding of edge-localized-modes (ELMs). Large ELMs with low-to-intermediate- $n$  peeling-ballooning (P-B) modes are significantly suppressed due to finite Larmor radius (FLR) effects when the ion temperature increases. For type-I ELMs, it is found from linear simulations that retaining complete first order FLR corrections as resulting from the incomplete “gyroviscous cancellation” in Braginskii’s two-fluid model is necessary to obtain good agreement with gyro-fluid results for high ion temperature cases ( $T_i \geq 3$  keV) when the ion density has a strong radial variation, which goes beyond the simple local model of ion diamagnetic stabilization of ideal ballooning modes. The maximum growth rate is inversely proportional to  $T_i$  because the FLR effect is proportional to  $T_i$ . The FLR effect is also proportional to toroidal mode number  $n$ , so for high  $n$  cases, the P-B mode is stabilized by FLR effects. Nonlinear gyro-fluid simulations show results that are similar to those from the two-fluid model, namely that the P-B modes trigger magnetic reconnection, which drives the collapse of the pedestal pressure. Due to the additional FLR-corrected nonlinear  $\mathbf{E} \times \mathbf{B}$  convection of the ion gyro-center density, for a ballooning-dominated equilibrium the gyro-fluid model further limits the radial spreading of ELMs. In six-field two fluid simulations, the parallel thermal diffusivity is found to prevent the ELM encroachment further into core plasmas and therefore leads to steady state L-mode profiles. The simulation results show that most energy is lost via ion channel during an ELM event, followed by particle loss and electron energy loss. Because edge plasmas have significant spatial inhomogeneities and complicated boundary conditions, we have developed a fast non-Fourier method for the computation of Landau-fluid closure terms based on an accurate and tunable approximation. The accuracy and the fast computational scaling of the method have been demonstrated. © 2013 AIP Publishing LLC. [<http://dx.doi.org/10.1063/1.4801746>]

## I. INTRODUCTION

This paper reports on the theoretical and simulation results of a Gyro-Landau-fluid (GLF) extension of the BOUT++ code<sup>1</sup> which contributes to increasing the physics understanding of edge-localized-modes (ELMs). The large ELMs with low-to-intermediate- $n$  peeling-ballooning (P-B) modes are significantly suppressed due to finite Larmor radius (FLR) effects when the ion temperature increases. Meanwhile, advanced GLF models with closure of high moments are necessary to simulate small ELMs with high- $n$  drift/resistive ballooning modes and to obtain self-consistent turbulence and transport between ELMs for the pedestal plasma profiles rebuild.

An isothermal truncation of the general electromagnetic gyro-fluid model of Snyder and Hammett<sup>2</sup> is developed for

ELM simulations. The ion gyrocenter density and electron density are combined to yield a gyro-kinetic vorticity density equation. The set of nonlinear electromagnetic gyro-fluid equations consists of gyro-kinetic vorticity density, ion gyro-center density, the generalized Ohms law, and Ampere’s law. The simple set of gyro-fluid equations correctly describes a range of plasma instabilities relevant to edge plasmas, such as low-to-intermediate- $n$  peeling-ballooning modes and high- $n$  drift-ballooning modes. The first-order Padé’s approximation to  $\Gamma_0(b) = 1/(1+b)$  is used to get the potential by inverting the gyrokinetic vorticity density in configuration space. In the limit of small ion gyro-radius length,  $b = k_{\perp}^2 \rho_i^2 \ll 1$  (to first order finite Larmor radius approximation in  $b$ ), this set of equations is shown to be the same as the two-fluid model that includes FLR effects. We demonstrate that the complicated nonlinear gyro-viscous tensor in the two-fluid model naturally appears in the isothermal gyro-fluid model as the FLR-corrected  $\mathbf{E} \times \mathbf{B}$  convection for the ion gyro-center density in the gyro-kinetic vorticity

<sup>a)</sup>Paper T13 2, Bull. Am. Phys. Soc. 57, 294 (2012).

<sup>b)</sup>Invited speaker.

density equation and the FLR-corrected gyro-kinetic vorticity density. This offers a simple, yet adequate description of ion dynamics that is relatively easy to implement in nonlinear simulation codes. We also show that the gyro-kinetic vorticity density is the charge density only in the cold-ion limit.

Because edge plasmas have significant spatial inhomogeneities and complicated boundary conditions, it is desirable to compute the closure terms in configuration space. The nonlocality of Landau-fluid operators can make the naive direct computations of the closure terms in configuration space via convolution or matrix multiplication very expensive. We have therefore developed a fast non-Fourier method for the computation of Landau-fluid closure terms based on an accurate and tunable approximation that can be numerically implemented through the solution of matrix equations in which the matrices are tridiagonal or narrowly banded. The accuracy, for the operator itself and for the resulting plasma response function and the fast computational scaling of the method have been demonstrated. A spectral collocation analysis has been developed that greatly aids in the optimization of the approximations for accuracy and computational cost, both for cases that are collisionless and for cases where collisional and collisionless damping processes compete.

As gyro-fluid code development proceeds, we also build the multi-field two-fluid codes in parallel to investigate additional important physics missing in the basic 3-field isothermal gyro-fluid model and to guide the multi-moment gyro-fluid extension that increases in accuracy to the kinetic equation. As it is well known that parallel Landau damping is important to microturbulence, we find that the parallel thermal diffusivities are large on the top of pedestal plasmas, which prevent the further encroachment of ELM perturbation into core plasmas and therefore leads to steady state L-mode profiles. This motivates us to develop a nonlocal parallel Gyro-Landau-fluid thermal transport model valid in all collisionality regimes.

The organization of this paper is as follows. The basic set of equations and isothermal simulation model are given in Sec. II. The 3-field and 6-field nonlinear simulations of peeling-ballooning modes are discussed in Sec. III. A new non-Fourier Method for applying the Landau-fluid operators is given in Sec. IV. Summary and discussion are given in Sec. V.

## II. AN ISOTHERMAL ELECTROMAGNETIC 3-FIELD GYRO-FLUID MODEL

To begin, we are interested in a simple 3-field gyro-fluid model that describes the finite Larmor radius (FLR) effects on early phase of ELM dynamics. In order to avoid complications associated with the sound wave, ion parallel motion, ion and electron Landau damping, and the interaction of kinetic Alfvén waves with drift waves, we assume that  $k_{\parallel}v_{ti} \ll \omega_{*i}$  and  $\beta_e \ll 1$ , where  $v_{ti}$  is the ion thermal velocity,  $\omega_{*i}$  is the ion drift frequency, and  $\beta_e$  is the ratio of the electron kinetic pressure to the magnetic pressures. The validity of the reduced model will be discussed in Sec. III B. The isothermal 3-field gyro-fluid model can be obtained from

Snyder-Hammett model<sup>2</sup> by (1) assuming constant temperatures for both the ions and electrons; (2) discarding all but the lowest-order moment for the ions and the lowest two parallel moments for the electrons; (3) ignoring compressibility of  $\mathbf{E} \times \mathbf{B}$  drift flow; (4) adding the cross term  $\nabla_{\perp} \ln n_i \cdot \nabla[(\Gamma_0 - \Gamma_1) \frac{e\phi}{T_0}]$  in the gyro-kinetic Poisson equation which is important for pedestal plasmas with large density gradient;<sup>3</sup> and (5) adding the current diffusion term with hyper-resistivity  $\eta_H$  in the generalized Ohm's law for magnetic reconnection in high-Lundquist number pedestal plasmas<sup>4</sup>

$$\frac{\partial n_{iG}}{\partial t} + \mathbf{v}_{EG} \cdot \nabla n_{iG} = - \left( \frac{2}{eB} \right) \mathbf{b}_0 \times \kappa \cdot \nabla p_{iG}, \quad (1)$$

$$\frac{\partial n_e}{\partial t} + \mathbf{v}_E \cdot \nabla n_e = \left( \frac{2}{eB} \right) \mathbf{b}_0 \times \kappa \cdot \nabla p_e - \nabla_{\parallel} (n_e v_{\parallel e}), \quad (2)$$

$$\frac{\partial A_{\parallel}}{\partial t} = -\partial_{\parallel} \phi + \frac{1}{n_e e} \partial_{\parallel} p_e + \frac{\eta}{\mu_0} \nabla_{\perp}^2 A_{\parallel} - \frac{\eta_H}{\mu_0} \nabla_{\perp}^4 A_{\parallel}, \quad (3)$$

$$J_{\parallel} = -\frac{1}{\mu_0} \nabla_{\perp}^2 A_{\parallel} = -n_e e v_{\parallel e}, \quad (4)$$

$$n_e = \bar{n}_i - n_i [1 - \Gamma_0(b)] \frac{Z_i e \phi}{T_0} + n_i \rho_i^2 (\nabla_{\perp} \ln n_i) \cdot \nabla_{\perp} \left[ (\Gamma_0 - \Gamma_1) \left( \frac{Z_i e \phi}{T_0} \right) \right], \quad (5)$$

$$\bar{n}_i = \Gamma_0(b)^{1/2} n_{iG}, \quad b = -\rho_i^2 \nabla_{\perp}^2, \quad (6)$$

where  $\bar{n}_i$  is the gyro-phase independent part of the real space ion density. The notation  $n_{iG}$  is the ion gyro-center density and  $n_i$  is the particle density (equal to  $n_e$  in the limit of small Debye length,  $k\lambda_D \ll 1$ ). For the various definitions of density, the relation between the particle and gyro-center representations is given by the gyro-kinetic Poisson equation, Eq. (5). Definitions of various quantities associated with plasma physics are as follows:

$$\begin{aligned} \mathbf{v}_{EG} &= \mathbf{b}_0 \times \nabla_{\perp} \Phi_G / B, & \mathbf{v}_E &= \mathbf{b}_0 \times \nabla_{\perp} \phi / B, \\ \tilde{\mathbf{B}} &= \nabla A_{\parallel} \times \mathbf{b}_0. \end{aligned} \quad (7)$$

The notation  $\Phi_G = \bar{\Phi} = \Gamma^{1/2}(b)\phi$  has been introduced for gyro-averaged electric potential. Here,  $\nabla_{\parallel} F = B \partial_{\parallel} (F/B)$  for any  $F$ ,  $\partial_{\parallel} = \partial_{\parallel}^0 + \tilde{\mathbf{b}} \cdot \nabla$ ,  $\tilde{\mathbf{b}} = \tilde{\mathbf{B}}/B$ ,  $\partial_{\parallel}^0 = \mathbf{b}_0 \cdot \nabla$ ,  $\kappa = \mathbf{b}_0 \cdot \nabla \mathbf{b}_0$ ,  $\eta$  is resistivity and  $\eta_H$  hyper-resistivity, which is equivalent to the electron viscosity  $\mu_{e\perp} = (n_e e^2 / m_e) \eta_H$ .<sup>5</sup> The symbol tilde represents the fluctuation quantities.

Since in the long wavelength regime of a quasi-neutral plasma  $\bar{n}_i$  and  $n_e$  are two large numbers and are almost equal  $\bar{n}_i \sim n_e$  and Eq. (5) can be rewritten as  $1 - \bar{n}_i/n_e \simeq (k_{\perp} \rho_i)^2 e\phi/T_e$ , where  $(k_{\perp} \rho_i)^2 \ll 1$  and  $e\phi/T_e \sim 1$ , the desired solution of Poisson equation as written depends on the difference of two large and almost equal numbers. Therefore, it is difficult to accurately obtain numerical solutions when  $n_{iG}$  and  $n_e$  evolve separately because the numerical errors in  $(\bar{n}_i(\mathbf{x}, t) - n_e(\mathbf{x}, t))$  may be on the same order as the ion polarization density.

Here, we propose an alternative formulation. We define two new variables: gyrokinetic vorticity density  $\varpi_G = eB(n_e - n_{iG})$

and gyrokinetic total pressure  $p_G = p_{iG} + p_e = n_{iG}T_{iG} + n_e T_e = (n_{iG} + n_e)T_0$ , assuming electron temperature  $T_e$  being equal to ion temperature  $T_{iG}$ ,  $T_e = T_{iG} = T_0$ . For the isothermal model, which neglects all considerations of temperature dynamics, we can rewrite the gyrokinetic vorticity density as

$$\frac{\partial \varpi_G}{\partial t} + \mathbf{v}_E \cdot \nabla \varpi_G - eB(\mathbf{v}_{EG} - \mathbf{v}_E) \cdot \nabla n_{iG} = 2\mathbf{b}_0 \times \kappa \cdot \nabla p_G + B \nabla_{||} j_{||}, \quad (8)$$

$$\frac{\partial p_G}{\partial t} + \mathbf{v}_E \cdot \nabla p_G + T_0(\mathbf{v}_{EG} - \mathbf{v}_E) \cdot \nabla n_{iG} = 0, \quad (9)$$

$$\varpi_G = eB \left\{ \Gamma_0^{1/2}(b)n_{iG} - n_{iG} - n_i[1 - \Gamma_0(b)] \left( \frac{Z_i e \phi}{T_0} \right) \right\} + n_i e B \rho_i^2 \nabla_{\perp} \ln n_i \cdot \nabla_{\perp} \left[ (\Gamma_0 - \Gamma_1) \left( \frac{Z_i e \phi}{T_0} \right) \right], \quad (10)$$

$$n_e = \frac{1}{2} \left( \frac{p_G}{T_0} + \frac{\varpi_G}{eB} \right), \quad n_{iG} = \frac{1}{2} \left( \frac{p_G}{T_0} - \frac{\varpi_G}{eB} \right), \quad p_e = n_e T_0. \quad (11)$$

Here, the parallel current term and the diamagnetic flow when  $T_i \neq T_e$  have been neglected in pressure equation. The collisional stress tensors and other higher order off-diagonal terms of the viscosity tensor can easily be included in connection to fluid descriptions. The equations for  $A_{||}$  and  $J_{||}$  are the same as in Eqs. (3) and (4). This formulation naturally couples different parallel/poloidal domains (core, the scrape-off-layer and the private flux region) together in the edge region through radial advection and gyroaverage. In principle, the vorticity formulation contains the same information as gyro-fluid Eqs. (1) and (2) because it is derived from them. Besides the numerical reason as discussed above, the vorticity Eq. (8) has the advantage of relative easily being generalized to a general vorticity equation with accurate physics for long wavelength and transport time scale phenomena like the self-consistent calculation of the radial electric field,<sup>6</sup> but this will be the subject of a future publication. Instead, in this study, we employ ion equilibrium with subsonic flow velocity  $v_i$ , which will be characterized by the force balance relation as discussed in Sec. II B.

### A. Gyro-fluid vorticity density equation in the limit of small ion gyro-radius length

In the long-wavelength limit, where  $(k_{\perp} \rho_i)^2 \ll 1$ ,  $\Gamma_0(b) = 1/(1+b) \simeq 1-b$ ,  $\Gamma_0^{1/2}(b) = 1/(1+b/2) \simeq 1-b/2$ ,  $\Gamma_0 - \Gamma_1 \simeq (1-b/2)/(1+b) \simeq 1-3b/2$ ,  $\Phi_G - \phi = (1/2)\rho_i^2 \nabla_{\perp}^2 \phi$ . The 3-field gyro-fluid model in the limit of small ion gyro-radius length becomes

$$\frac{\partial \varpi_G}{\partial t} + \mathbf{v}_E \cdot \nabla \varpi_G - \frac{eB}{2T_0} \rho_i^2 \left[ \frac{\mathbf{b}_0 \times \nabla_{\perp} (\nabla_{\perp}^2 \phi)}{B} \right] \cdot \nabla p_{iG} = 2\mathbf{b}_0 \times \kappa \cdot \nabla p_G + B \nabla_{||} j_{||}, \quad (12)$$

$$\frac{\partial p_G}{\partial t} + \mathbf{v}_E \cdot \nabla p_G + \frac{1}{2} \rho_i^2 \left[ \frac{\mathbf{b}_0 \times \nabla_{\perp} (\nabla_{\perp}^2 \phi)}{B} \right] \cdot \nabla p_{iG} = 0, \quad (13)$$

$$\varpi_G = \frac{eB}{T_0} \rho_i^2 \left[ n_i Z_i e \nabla_{\perp}^2 \phi + n_i Z_i e \nabla_{\perp} \ln n_i \cdot \nabla_{\perp} \phi + \frac{1}{2} \nabla_{\perp}^2 p_{iG} \right]. \quad (14)$$

The equations for  $A_{||}$ ,  $J_{||}$ ,  $n_e$ ,  $n_{iG}$ , and  $p_e$  are the same as Eqs. (3), (4), and (11), respectively. By defining the two-fluid vorticity density  $\varpi = \omega_{ci} [\varpi_G + (eB/2T_0)\rho_i^2 \nabla_{\perp}^2 p_{iG}]$ , this equation can be rewritten into the form which is the same as two-fluid version of vorticity equation (2) given by Xu *et al.*,<sup>7</sup> excluding external momentum sources and collisional ion viscosity, which is given here again for comparison and will be later referred as two-fluid model in simulation sections

$$\frac{\partial \varpi}{\partial t} + (\mathbf{v}_E + v_{||i} \mathbf{b}_0) \cdot \nabla \varpi = (2\omega_{ci}) \mathbf{b}_0 \times \kappa \cdot \nabla p + n_i Z_i e \frac{4\pi v_A^2}{c^2} \nabla_{||} j_{||} - \frac{1}{2} \{ n_i Z_i e \mathbf{v}_{pi} \cdot \nabla (\nabla_{\perp}^2 \phi) + \mathbf{v}_E \cdot \nabla (\nabla_{\perp}^2 p_i) - \nabla_{\perp}^2 [\mathbf{v}_E \cdot \nabla (p_i)] \}. \quad (15)$$

It should be noted, however, that Eq. (15) is written in CGS units as the original paper,<sup>7</sup> while SI units are used in this paper. This resolves the long-standing issue regarding the difference in vorticity equation derived from two-fluid and gyrokinetic framework. The gyro-viscous terms emerge naturally from the FLR nonlinearities in the ion gyrocenter density in the limit of small ion gyro-radius length. Furthermore, the gyro-fluid equations show a simple physics picture and can be easily implemented in simulation codes. The one-half of ion diamagnetic drift vorticity in  $\varpi_G$  [the last term on the right-hand-side of Eq. (14)] indicates that the gyro-kinetic vorticity density  $\varpi_G$  is the charge density only in the cold-ion limit.

### B. Gyro-fluid equilibrium and axisymmetric component of fluctuations

Ion equilibrium with subsonic flow velocity,  $\mathbf{v}_i$ , can be characterized by the force balance relation  $n_i Z_i e \nabla \Phi + \nabla P_i = Z_i e n_i \mathbf{v}_i \times \mathbf{B}$ . The parallel two-fluid vorticity (or simply two-fluid vorticity)  $\varpi = \omega_{ci} \mathbf{b} \cdot \nabla \times (n_i m_i \mathbf{v}_i)$  therefore can be written as  $\varpi = n_i Z_i e \nabla_{\perp}^2 \Phi + n_i Z_i e \nabla_{\perp} \ln n_i \cdot \nabla_{\perp} \Phi + \nabla_{\perp}^2 P_i$ . For a typical ion equilibrium with subsonic ion flow velocity and with weak ion temperature gradient in H-mode pedestal plasmas, the  $\mathbf{E} \times \mathbf{B}$  drift is balanced with ion diamagnetic drift, the equilibrium vorticity is almost zero,  $\varpi_0 \simeq 0$ , which yields the isothermal relation  $Z_i e \Phi_0 \simeq T_0 \ln P_{i0}$ .

Therefore, to lowest order of the poloidal ion gyroradius to the ion temperature scale ( $\rho_{pi}/L_{Ti} \ll 1$ ), subsonic ion flow implies that the pedestal is maintained by a large electron current with the ions electrostatically confined. Since the two-fluid vorticity is different from gyro-fluid vorticity by one-half of ion diamagnetic drift vorticity, typical subsonic ion flow force balance means a non-zero gyro-fluid equilibrium vorticity

$$\varpi_{G0} = - \left( \frac{eB}{2T_0} \right) \rho_i^2 \nabla_{\perp}^2 P_{i0}. \quad (16)$$

Similarly for the isothermal model, if we assume that the turbulence-generated steady-state axisymmetric component

of ion flow is subsonic ( $\langle v_{i\perp} \rangle_\zeta \ll v_{Ti}$ ), the same isothermal relation holds for gyro-fluid model as well  $Z_i e \Phi \simeq T_0 \ln(P_{i0} + \langle p_i \rangle_\zeta)$ . Here,  $\langle p_i \rangle_\zeta$  means the axisymmetric component of ion pressure fluctuations, i.e.,  $n=0$  component. The same is true for the turbulence-generated axisymmetric component of gyro-fluid vorticity

$$\langle \varpi \rangle_\zeta = 0 \quad \Rightarrow \quad \langle \varpi_G \rangle_\zeta = - \left( \frac{eB}{2T_0} \right) \rho_i^2 \nabla_\perp^2 \langle p_{iG} \rangle_\zeta. \quad (17)$$

In other words, we assume that the ion response is adiabatic for both equilibrium and steady-state axisymmetric component of fluctuations.

### III. SIMULATIONS OF EDGE-LOCALIZED-MODES

To study the physics of nonlinear P-B mode dynamics, we choose circular cross-section toroidal equilibria with an aspect ratio of 2.9 generated by the TOQ equilibrium code. The plasma equilibrium is far above the marginal P-B instability threshold with a pedestal toroidal pressure  $\beta_{t0} = 1.941 \times 10^{-2}$  and a normalized pedestal width  $L_{ped}/a = 0.0486$ .<sup>8</sup> This is a simple circular equilibrium which has been designed for use in code verification and physics exploration. It is not meant to represent a particular experimental case, but rather is an example case with a strongly unstable pedestal in simple geometry. This equilibrium has been used in previous code verification exercises, and it is described in detail in Ref. 8. It is worth noting that in experimental reconstructions, both the bootstrap current as well as the Ohmic (and usually insignificant driven) current are included. The bootstrap current is generally the largest component, and so for simple test equilibria such as this one, one can use a bootstrap current profile to get a typically shaped current profile across the edge region.

In this section, a series of gyro-fluid and two-fluid simulations are conducted to investigate the scaling characteristics of the ELMs as a function of ion temperature and density. During the scan the pressure profile and the magnetic equilibrium are kept the same. Therefore the bootstrap current is kept the same as the base case ( $T_{base} = 3$  keV). Because BOUT++ code reads the bootstrap current from the equilibrium file, which is generated by the TOQ equilibrium code, other equilibrium files are not currently available. Nevertheless, since the bootstrap current drive is small for the base case, we label it as a ballooning-dominated equilibrium. It is anticipated that the impact of the bootstrap current on the scan is small as well, or at least for cases  $T_0 = T_{i0} = T_{e0} < T_{base} = 3$  keV where bootstrap current becomes even smaller.

In this study, both equilibrium flow and turbulent zonal flow have been set to be zero for both two-fluid and gyro-fluid models in BOUT++ code:  $\mathbf{V}_0 = \mathbf{V}_{E0} + \mathbf{V}_{\nabla P_i} = 0$  and  $\langle \delta \mathbf{v} \rangle_\zeta = \langle \mathbf{v}_E \rangle_\zeta + \langle \mathbf{v}_{\nabla P_i} \rangle_\zeta = 0$ . Therefore, the equilibrium electric field is  $E_{r0} = (1/n_0 Z_i e) \nabla_r P_{i0}$  with ion pressure  $P_{i0} = P_0/2$ , and the perturbed electric field is  $\langle E_r \rangle_\zeta = (1/n_0 Z_i e) \nabla_r \langle P_i \rangle_\zeta$ . The zonal magnetic field is also set to be zero as it is negligibly small compared to the equilibrium magnetic field  $B_0$ . The influence of equilibrium shear flow on peeling-ballooning instabilities and edge localized mode crashes can be found in a previous publication.<sup>10</sup>

Radial boundary conditions used are  $\varpi_G = 0, \partial p_G / \partial \psi = 0$  for gyro-fluid and  $\varpi = 0, \partial p / \partial \psi = 0$  for two-fluid,  $\nabla_\perp^2 A_\parallel = 0$ , and  $\partial \phi / \partial \psi = 0$  on inner radial boundary;  $\varpi_G = 0, p_G = 0$  for gyro-fluid and  $\varpi = 0, p = 0$  for two-fluid,  $\nabla_\perp^2 A_\parallel = 0$ , and  $\phi = 0$  on outer radial boundary. The domain is periodic in parallel coordinate  $y$  (with a twist-shift condition) and periodic in binormal coordinate  $z$ . For efficiency, when performing nonlinear simulations, only 1/5th of the torus is simulated. The number of grid cells in each coordinate are  $n_\psi = 512, n_y = 64$ , and  $n_z = 32$ .

From the given magnetic geometry and plasma profiles with edge pedestal structures, the simulation is initialized with a small  $n=15$  vorticity perturbation with Gaussian shape in radial and poloidal direction. The fastest growing mode dominates the initial phase of the calculation, in which the perturbation grows at an approximately exponential rate due to the P-B modes. After this initial linear phase, the perturbation evolves to a nonlinear saturated state, a pedestal collapsing phase, and a new sustained turbulent state without edge pedestal structures.

#### A. ELM 3-field gyro-fluid simulations

Utilizing a Padé approximation for the modified Bessel functions, this set of equations (3), and (8) and (9) with the auxiliary equations (4), (10) and (11), (16) and (17) is implemented in the BOUT++ framework with full ion FLR effects, except that  $\Gamma_0 - \Gamma_1 \simeq 1$  is used in the last term of Eq.(10) for ELM simulations, where we assume  $k_\perp L_n \gg 1$ . This simple isothermal 3-field gyro-fluid model does not yet include Landau damping for peeling-ballooning (P-B) modes with  $\omega \sim \omega_{*i} \gg \omega_{ii}$ , where  $\omega_{*i}$  is the ion diamagnetic drift frequency and  $\omega_{ii} = v_{ii}/qR$  is the thermal ion transit frequency.

In this section, the resistivity  $\eta$ , hyper-resistivity,  $\eta_H$ , and edge temperature  $T_0$  are treated as constants in space-time across simulation domain.

##### 1. Linear 3-field gyro-fluid simulations

The initial simulation results are shown to be consistent with the previous two-fluid model including only the ion diamagnetic drift for constant density profile. Retaining the complete first-order FLR corrections (including all three terms on the second line of Eq. (15)) is necessary to obtain good agreement with gyro-fluid results for high ion temperature cases ( $T_i \gtrsim 3$  keV) when the ion density has a strong radial variation. The influence of gyro-radius effects on the linear growth rate of P-B modes vs.  $n$  (top) and  $k_\theta \rho_i$  (bottom, calculated with  $T_i = 1$  keV) is summarized in Fig. 1 for type-I ELMs. Good agreement in the linear growth rate is shown in long-wavelength limit among the ideal MHD model (black), two-fluid model (solid), and gyro-fluid model (dash). In both cases, the maximum growth rate is inversely proportional to  $T_i$  because the FLR effect is proportional to  $T_i$ . The FLR effect plays the role of a threshold in the growth rate. Only the perturbations with a growth rate higher than the threshold become unstable. Therefore, as the ion temperature increases, the FLR and the stabilizing effect increase. The FLR effect is also proportional to toroidal mode number  $n$ ,



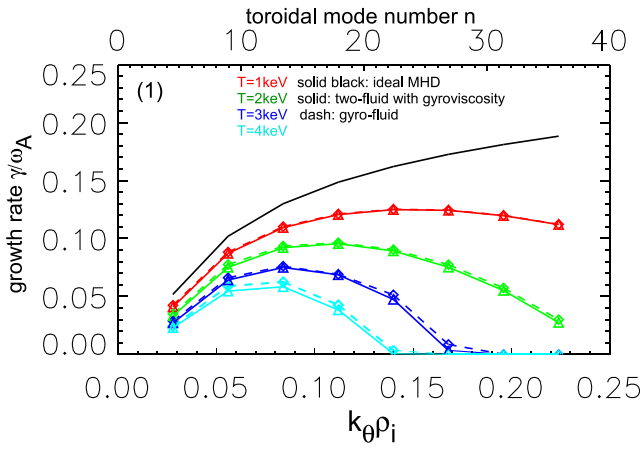


FIG. 1. The influence of the FLR physics on the linear growth rate of P-B modes versus toroidal mode number  $n$  (top) or poloidal wavelength normalized to ion Larmor radius  $k_\theta \rho_i$  (bottom), calculated with  $T_0 = 1$  keV for the ideal MHD P-B mode (black), with two-fluid retaining the complete first-order FLR corrections (solid), and with gyro-fluid full FLR effects (dash) for different plasma temperature  $T_i$ . The growth rates are normalized to the Alfvén frequency  $\omega_A$ , where  $\omega_A = v_A/R_0$  and  $v_A$  is the Alfvén velocity and  $R_0$  is the major radius.

so for high  $n$  cases, the peeling-ballooning mode is stabilized by FLR effects.

## 2. Nonlinear 3-field gyro-fluid simulations

Nonlinear gyro-fluid simulations show results that are similar to those from the two-fluid model, namely that the P-B modes trigger magnetic reconnection, which drives the collapse of the pedestal pressure.<sup>4,9</sup> Hyper-resistivity is found to limit the radial spreading of ELMs by facilitating magnetic reconnection. However, as shown in Fig. 2, variation by three orders of magnitude in hyper-resistivity leads to variation of less than a factor of two in ELM size. The ELM size is found to be weakly sensitive to the hyper-resistivity for large ELMs. For a fixed hyper-resistivity  $S_H = 10^{12}$ , when  $S > S_c = \sqrt{S_H \omega_A / \gamma} > 10^6$ , which is relevant to today's modestly sized tokamaks and ITER, our

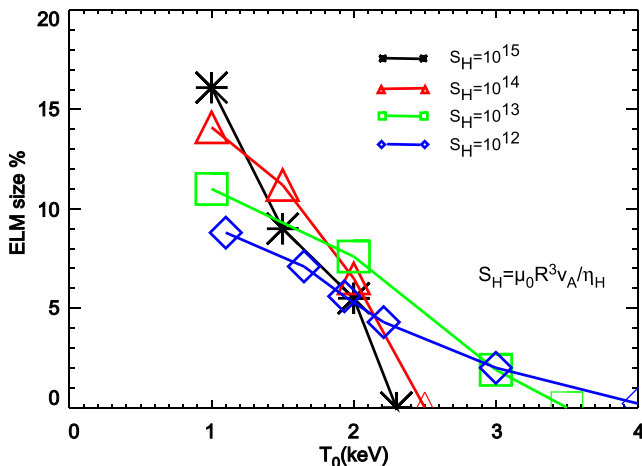


FIG. 2. ELM size vs ion temperature  $T_i$  and hyper-resistivity  $\eta_H$  for constant density case. Lundquist number  $S = \mu_0 R_0 v_A / \eta = 10^8$  and hyper-Lundquist number  $S_H = \mu_0 R^3 v_A / \eta_H$ . The plasma current drive and magnetic equilibrium are fixed during the scan.

previous simulations find that the ELM size is insensitive to the resistivity.<sup>9</sup> Due to the additional FLR-corrected nonlinear  $E \times B$  convection for the ion gyro-center density, the gyro-fluid model further limits the radial spreading of ELMs as shown in Fig. 2, and for a ballooning-dominated equilibrium the FLR effect can significantly decrease the ELM size when the pedestal ion temperature increases from 1 keV to 4 keV because high- $n$  modes are stabilized. Here the Lundquist number  $S = \mu_0 R v_A / \eta = 10^8$ , the hyper-Lundquist number  $S_H = \mu_0 R^3 v_A / \eta_H$ ,  $v_A$  is the Alfvén velocity, and  $R$  is the major radius. The ELM size is defined as  $\Delta_{ELM} = \Delta W_{PED} / W_{PED} = \int_{R_{in}}^{R_{out}} \oint dR d\theta (P_0 - \langle P \rangle_\zeta) / \int_{R_{in}}^{R_{out}} \oint dR d\theta P_0$ , the ratio of the ELM energy loss ( $\Delta W_{PED}$ ) to the pedestal stored energy  $W_{ped}$ . Here,  $P$  is the pedestal pressure and the symbol  $\langle \rangle_\zeta$  means the average over bi-normal periodic coordinate. The lower integral limit is the pedestal inner radial boundary  $R_{in}$ , while the upper limit is the radial position of the peak pressure gradient  $R_{out}$ .

## B. Nonlinear 6-field two-fluid simulations

In Sec. III A, we presented 3-field isothermal gyro-fluid and two-fluid models to simulate ELM dynamics, which include the fundamental physics: (1) peeling-ballooning instability; (2) ion diamagnetic stabilization of high- $n$  ballooning modes; and (3) resistivity and hyper-resistivity for magnetic reconnection and ELM crashes. The question naturally arises how the additional physics affects the basic ELM models. Therefore, we have extended the basic 3-field model to sophisticated multi-field models: (1) four-field model<sup>11</sup> with vorticity  $\varpi$ , total pressure  $P$ , parallel vector potential  $A_{||}$ , and ion parallel velocity  $V_{||}$ , which include sound waves; (2) five-field model<sup>12,13</sup> with vorticity  $\varpi$ , density  $n$ , ion and electron temperature  $T_{i,e}$ , and parallel vector potential  $A_{||}$ , which include parallel thermal diffusivities; and (3) six-field model<sup>14</sup> based on Braginskii equations in drift ordering with vorticity  $\varpi$ , density  $n$ , ion and electron temperature  $T_{i,e}$ , parallel vector potential  $A_{||}$ , and ion parallel velocity  $V_{||}$ .

In these five-field and six-field models, nonlinear parallel thermal diffusivities and nonlinear resistivity are used. Due to the strong spatial variation of the plasma density and temperature profiles in the edge pedestal across the separatrix, we use the following flux-limited expression for parallel thermal diffusivity in a harmonic average form:<sup>15</sup>  $\chi_{||j}^{eff} = (1/\chi_{||j}^{SH} + 1/\chi_{||j}^{FS})^{-1}$ ,  $j = e, i$ , where  $\chi_{||e}^{SH} = 3.2 v_{th,e}^2 / \nu_e$ ,  $\chi_{||i}^{SH} = 3.9 v_{th,i}^2 / \nu_i$ , and  $\chi_{||j}^{FS} \simeq \alpha_j v_{th,j} q_{95} R_0$ . Under collisional conditions, the Spitzer-Harm expressions  $\chi_{||j}^{SH}$  clearly apply. In the opposite collisionless or long mean free path limit, the heat flux saturates at the one-way free-streaming value  $\chi_{||j}^{FS}$ , where  $\alpha_j$  is the flux-limiting coefficient, i.e., the ratio between free-streaming and actual heat fluxes in the collisionless limit. A number of studies using kinetic simulations have produced widely disparate values for  $\alpha_j$ , ranging from 0.03 to 3.<sup>16</sup> Here, we assume  $\alpha_j = 1$ . Clearly the accuracy of such a flux-limiting coefficient is not high although better nonlocal Gyro-Landau-fluid models are under development by extending the Landau-fluid operator to collisional regime

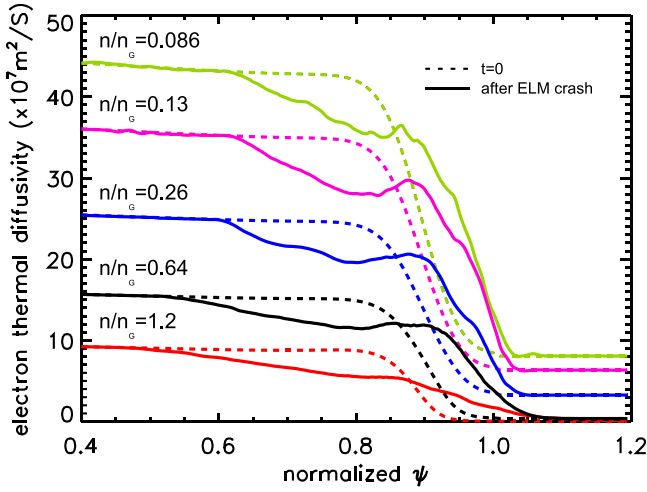


FIG. 3. Radial profiles of electron parallel thermal diffusivity for different separatrix density at the beginning of the simulation ( $t=0$ , dashed curve) and after the ELM crash (solid curve). Here  $q_{95} = 5$  is used to calculate the free streaming value.

using the fast non-Fourier approach as discussed in Sec. IV. From 5-field and 6-field simulations, we typically find that the parallel thermal diffusivities are large on the top of pedestal, as in shown Fig. 3, which prevent the further encroachment of ELM perturbation into core plasmas and, therefore, leads to steady state L-mode profiles, as indicated by the radial profiles of parallel thermal diffusivity after an ELM crashes (solid curve,  $\propto \sqrt{\langle T_e \rangle_{\zeta}}$ ).

In 6-field model, the equilibrium pressure profile  $P_0$  is separated into ion density  $n_{i0}$ , ion and electron temperature,  $T_{i0}$  and  $T_{e0}$ . For a given pressure, we partition it between density and temperature, select representative density profiles  $n_{i0}$  using the following analytical formula, and then back out the temperature using the relation  $T_{i0} = T_{e0} = P_0 / (2n_{i0})$ :

$$n_{i0}(x) = \frac{(n_{height} \times n_{ped})}{2} \left[ 1 - \tanh\left(\frac{x - x_{ped}}{\Delta x_{ped}}\right) \right] + n_{ave} \times n_{ped}. \quad (18)$$

Here,  $n_{ped}$  is the ion number density on the top of the pedestal region,  $n_{ave}$  is the ratio to control the bottom amplitude of  $n_{i0}$  outside the separatrix, and  $n_{height}$  is the coefficient to specify the gradient of  $n_{i0}$ . The variables  $x_{ped}$  and  $\Delta x_{ped}$  represent the position of peak gradient and the width of pedestal region of  $P_0$ , respectively. The location of the separatrix is the normalized poloidal flux  $\psi_n = 1.0$ . The density profile  $n_{i0}$  is set to be a constant value outside the separatrix. The simulation results in the Table I are obtained for equilibrium

profiles using the parameters  $n_{height} = 0.55$  and  $n_{ave} = 0.2$ , so  $T_{e0} = 1.2$  keV at the inner boundary and  $T_{e0} = 48$  eV in the scrape-off layer plasmas. For 3-field model, we use the ideal running option plus diamagnetic drift, normalized resistivity with Lundquist number  $S = 10^8$ , additional gyroviscous terms defined in the second line of Eq. (15), and the same density profile  $n_{i0}$ . For 6-field, the full Braginskii's two-fluid model is used as defined in Ref. 14 with Spitzer-Harm resistivity profile.

With all additional physics added, such as ion acoustic waves, parallel thermal diffusivities, Hall effect, toroidal compressibility, and electron-ion friction, for the same plasma equilibrium as described in the beginning of Sec. III A, we find that the change of the linear growth rate for most unstable modes is less than 20% in comparison with the results of the basic 3-field two-fluid model although the 6-field model shifts the instability threshold from  $n = 3$  of 3-field model to  $n = 4$  of 6-field model for low- $n$  modes and shifts stable threshold from  $n = 100$  of 3-field to  $n = 80$  of 6-field model for high- $n$  modes, as shown in Table I. Here, the differences of linear growth rates for different mode number  $n$  between these two models are listed. The ELM size at the saturation phase is also listed in this table and the difference of two models is 1.4%.

Therefore, the 3-field two-fluid model is good enough to qualitatively understand the ELM thresholds due to P-B modes and quickly simulate early phase of ELM crashes with strongly unstable pedestals. However, ELM dynamics is a multi-scale problem, ranging from meso-scale MHD events to micro-scale turbulent dissipation due to electron gyro-radius effects. In order to simulate a ELM cycle and perform experimental validations, sophisticated multi-field models are necessary to obtain (1) ELM power loss via separate ion and electron channels; (2) ELM power depositions on plasma facing components (PFCs); and (3) self-consistent turbulence and transport between ELMs for the pedestal profiles rebuild. From six-field simulations, we find that most energy is lost via ion channel during an ELM event, followed by particle loss and electron energy loss, as shown in Fig. 4. Furthermore, Fig. 4(b) show results of density scan for a fixed pressure profile with a ballooning-dominated equilibrium: higher density leads to large ELM size during an ELM event because of reduced ion diamagnetic stabilization and parallel thermal conduction from lower temperature.

For a fixed pressure profile, when density  $n$  increases and temperature ( $T_e, T_i$ ) decrease, thermal diffusivities ( $\chi_{||ie}^{eff}$ ) and parallel damping decrease as well. Therefore, the pedestal profiles collapse further into core plasmas, which lead to

TABLE I. Linear growth rate  $\gamma$  vs toroidal mode number  $n$  and poloidal wavelength normalized to ion Larmor radius  $k_0 \rho_i$  (calculated with  $T_i = 600$  eV at peak gradient position), ELM size, and their differences between the fundamental 3-field and 6-field Braginskii's two-fluid model. The growth rates are normalized to the Alfvén frequency  $\omega_A$ , where  $\omega_A = v_A/R_0$  and  $v_A$  is the Alfvén velocity and  $R_0$  is the major radius.

$N$	3	4	10	15	30	45	60	80	100	ELM size %
$k_0 \rho_i$	0.015	0.020	0.051	0.076	0.152	0.228	0.304	0.405	0.506	...
$\gamma_{3-field}/\omega_A$	0.044	0.106	0.263	0.336	0.401	0.358	0.222	0.061	0	14.8
$\gamma_{6-field}/\omega_A$	0	0.032	0.211	0.287	0.361	0.313	0.190	0	0	14.6
Difference %	...	...	19.8	12.6	10.0	12.6	14.4	...	...	1.4

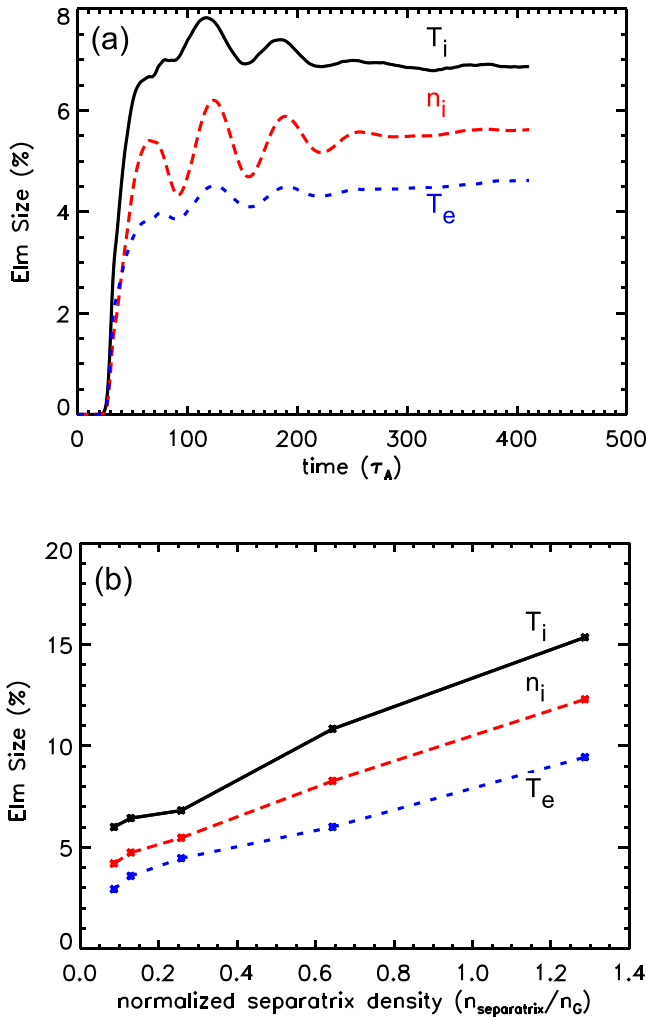


FIG. 4. (a) The time history of the ELM loss fraction ( $\Delta W_{ped}/W_{ped}$ ) or ELM size calculated from ion temperature (solid curve), density (dashed curve) and electron temperature (dotted curve) for  $n/n_G = 0.26$ . (b) The ELM loss fraction ( $\Delta W_{ped}/W_{ped}$ ) or ELM size vs normalized separatrix density  $n_{\text{separatrix}}/n_G$ , where  $n_G = I_p/\pi a^2$ . The plasma current drive and magnetic equilibrium are fixed during the scan.

larger ELM size. However, the opposite trend of the elm size vs density or temperature is observed in experiments.<sup>17,18</sup> We provide some cautions and two caveats on comparing simulation results with these experimental observations for the density or temperature scan. (1) The simulation results are valid for a ballooning-dominated equilibrium with a fixed bootstrap current; while experimental scan involves transitions from ballooning-dominated to peeling-dominated equilibrium and vice versa, the change of bootstrap current with collisionality during the scan leads to changes of the magnetic equilibrium. (2) During the simulation scan, the pressure profile and pedestal stored energy are fixed, while during a experimental scan, higher temperature typically means higher pedestal stored energy, which leads to more ELM energy loss. Finally, it is worth noting that for the range of temperature (density) variation scanned in simulations, pedestal plasma is still in the weakly collisional limit; therefore, as pedestal temperature decreases, the decreasing of thermal diffusivity ( $\chi_{||i,e}^{eff}$ ) is mainly from the free-streaming contribution  $\chi_{||i}^{FS}$ , as shown in Fig. 3.

#### IV. A NEW NON-FOURIER METHOD FOR APPLYING THE LANDAU-FLUID OPERATORS

Tokamak edge plasma regimes both necessitate the implementation of Landau-fluid (LF) operators<sup>19,20</sup> in edge-plasma fluid codes, such as BOUT++, and also present new challenges to existing approaches for doing so. On the one hand, kinetic effects are important. However, significant spatial inhomogeneities and complicated boundary conditions are also present, which pose significant difficulties for the standard Fourier implementations.

We have, therefore, developed a “fast” configuration-space-based, non-Fourier, approach for the application of these operators, which has Fourier-like computational scaling. This approach is based on an approximation of  $1/|k|$  by a sum of Lorentzians

$$\frac{1}{|k|} \approx \beta \sum_{n=0}^{N-1} \frac{\alpha^n k_0 \xi_n}{k^2 + (\alpha^n k_0)^2}. \quad (19)$$

Suitable choices of constants  $\alpha$ ,  $\beta$ ,  $\xi_n$ ,  $k_0$ , and  $N$  allow for a very good fit in Fourier space of the sum to  $1/|k|$  over a wide range of the wavenumber  $k$ . A detailed method and implementation description has been presented<sup>21</sup> and will be given in a future publication.

The key feature of the approximation in Eq. (19) is that the Lorentzians can be interpreted as real-space Helmholtz-equation solutions, which can be numerically implemented using highly efficient linear solvers. The  $|k_{||}|$  Landau-fluid closure has been implemented with the existing solvers in BOUT++, and implementation of the toroidal  $|\omega_d|$  closure<sup>20</sup> is underway using slightly modified versions of the perpendicular solvers available in BOUT++.

A theory and a constructive procedure for optimizing approximations of the kind in Eq. (19) based on spectral collocation has been developed, including extensions to the operators involved in the collisional case.<sup>20</sup> In order to better understand the approximation, consider the simplified infinite sum

$$S(|k|, \alpha) \equiv \sum_{n=-\infty}^{\infty} \frac{\alpha^n k_0}{k^2 + (\alpha^n k_0)^2}. \quad (20)$$

For each value of  $k$ , this sum converges to a finite value which satisfies

$$S(\alpha|k|, \alpha) = \frac{1}{\alpha} S(|k|, \alpha). \quad (21)$$

Thus, a simple truncation of the infinite sum of Eq. (20), which gives the expression on the right hand side of Eq. (19) with  $\xi_n = 1$ , can be expected to yield a reasonable approximation. The ratio of this expression to  $1/|k|$ , i.e.,  $|k| \beta \sum_{n=0}^{N-1} \alpha^n k_0 \xi_n / [k^2 + (\alpha^n k_0)^2]$  is shown as the red curve in Fig. 5(a) for  $N = 7$ ,  $\alpha = 5$ ,  $\beta = 1.04$ , and  $k_0 = 1$ . The collocation analysis allows for a more general choice of  $\xi_n$  and optimizes this choice by requiring that the sum in Eq. (19) agrees exactly with the target expression  $1/|k|$  at a suitably chosen set of collocation points ( $k$  values). An improved fit,

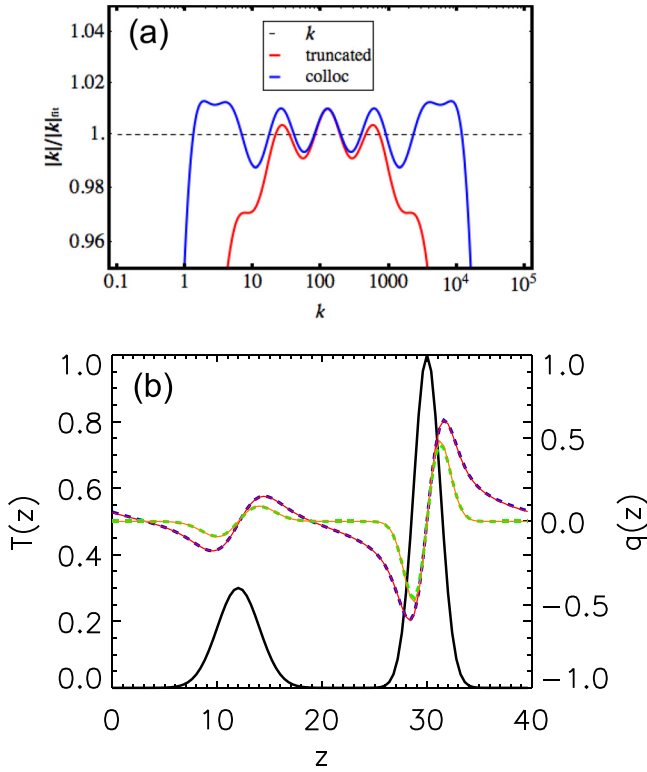


FIG. 5. (a) Ratio of actual value of  $|k|$  to fit using a sum of 7 scaled Lorentzians. The “truncated” curve is for a simple truncation fit, while the “colloc” curve is for an improved fit from the collocation analysis. (b) Comparison of the nonlocal flux resulting from a temperature profile (black solid). The curves are nonlocal flux computed with the sum of Lorentzians (blue dashed), and Fourier method (red), and the local (diffusive) flux computed with finite differences (green dashed), and the Fourier method (orange).

easily obtained by this procedure, still with  $N=7$  and  $\alpha=5$ , and hence essentially the same computational cost in a numerical implementation, is shown as the blue curve in Fig. 5(a). It is seen that the collocation procedure improves the spectral range of excellent fit by a factor of 100, yielding a fit with a very small ( $\sim 1.5\%$ ) relative error over a very large spectral range ( $\sim 5 \times 10^3$ ). Fig. 5(b) shows that the nonlocal flux computed using this method with an implementation of the Lorentzian terms as solutions of Helmholtz equations using a finite difference discretization and tridiagonal matrices gives excellent agreement with the result from the spectral method.

To gain confidence of the non-Fourier Lorentzian approach, further tests are done for the standard linear benchmark of the so-called Cyclone base case using Ottaviani gyro-fluid model:<sup>22</sup> the growth rate of the Ion Temperature Gradient mode (ITG) as a function of the poloidal wave vector  $k_\theta \rho_i$ . The Cyclone base case parameters<sup>23</sup> are safety factor  $q=1.4$ , magnetic shear  $s=0.78$ , inverse aspect ratio  $r/R=0.19$ , normalized temperature gradient length  $R/L_T=6.9$ , normalized density gradient length  $R/L_N=2.2$ , electron to ion temperature ratio  $T_e/T_i=1$ , electrostatic, and adiabatic electrons. The growth rate for this case is shown in Fig. 6 as a function of the normalized poloidal wave vector ( $k_\theta \rho_i$ ) with (red curves) and without Landau-damping (blue curves) calculated with both BOUT++ code (solid curve) and global ITG eigenvalue solver (dashed curve) with  $\nabla_{||}$  operator using Fourier Method. As can be seen from the figure, good agreement is obtained.

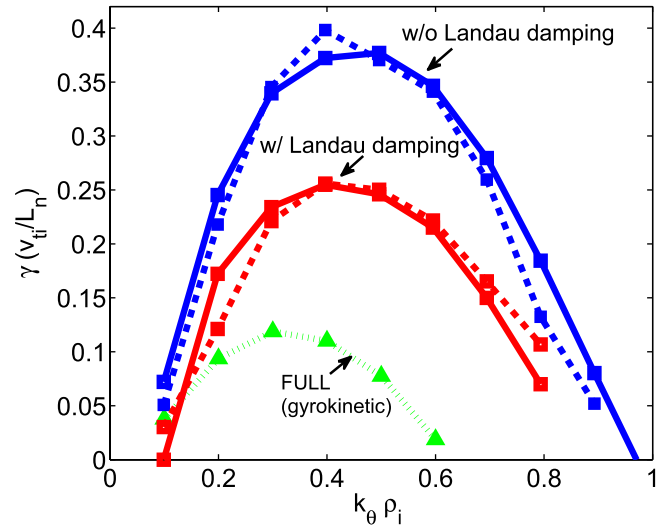


FIG. 6. For Ottaviani physics model using parameters of cyclone base case, the solid lines are the results from BOUT++ code using the Lorentzian method, while the dashed lines are the results from eigenvalue solver. The dotted curve is from gyrokinetic code. The spectral shift parameter  $k_0=0.05/qR$ , where  $q=rB_i/RB_p$  is the local safety factor, and  $r$  is the local minor radius.  $N=7$ ,  $\alpha=5$ ,  $\beta=1.04$ , and  $\xi_n=1$ .

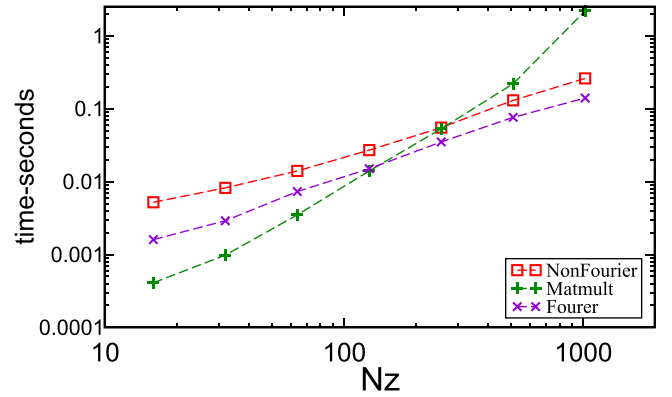


FIG. 7. Computational time versus the number of grid cells in a periodic domain for the sum of Lorentzians (non-Fourier), direct matrix multiplication (Matult), and Fourier approaches.

The addition of the parallel Landau-damping closure in Cyclone-base case simulations brings the curve (red curve) of the linear growth rate vs. toroidal wavenumber into better agreement with the gyrokinetic results (dotted curve) than in the absence of this closure (blue curve). It is anticipated that the inclusion of the toroidal closure will further greatly improve the level of agreement.

We have implemented and compared the computational cost of this and other approaches. Fig. 7 shows that the fast non-Fourier approach has a computational cost scaling for large numbers of grid cells similar to the Fourier approach. For modest numbers of grid cells, ( $<100$ ), direct matrix multiplication is a viable alternative and can be more efficient than even the Fourier approach.

## V. SUMMARY AND DISCUSSIONS

In conclusion, an isothermal electromagnetic 3-field gyro-fluid model [Eqs. (3) and (8), and (9) with the auxiliary



equations (4), (10) and (11), (16) and (17)] has been developed and implemented in the BOUT++ framework to study the physics of nonlinear peeling-ballooning mode dynamics. It is found from linear simulations that retaining complete first order FLR corrections as resulting from the incomplete “gyroviscous cancellation” in Braginskii’s two-fluid model [i.e., including all three terms on the second line of Eq. (15)] is necessary to obtain good agreement with gyro-fluid results for high ion temperature cases ( $T_i \geq 3\text{keV}$ ) when the ion density has a strong radial variation, which goes beyond the simple local model of ion diamagnetic stabilization of ideal ballooning modes. Nonlinear gyro-fluid simulations show results that are similar to those from the two-fluid model, namely that the P-B modes trigger magnetic reconnection, which drives the collapse of the pedestal pressure. Hyper-resistivity is still required in gyro-fluid simulations to facilitate magnetic reconnection. Due to the additional FLR-corrected nonlinear  $\mathbf{E} \times \mathbf{B}$  convection for the ion gyro-center density, for a ballooning-dominated equilibrium, the gyro-fluid model further limits the radial spreading of ELMs, and the FLR effect can significantly decrease the ELM size when the pedestal ion temperature increases from 1 keV to 4 keV because high- $n$  modes are stabilized.

The multi-field two-fluid simulations, including additional physics such as ion acoustic waves, parallel thermal diffusivities, Hall effect, toroidal compressibility, and electron-ion friction, show that the change of the peak linear growth rate is less than 20% in comparison with the results of the basic 3-field two-fluid model. The difference of ELM size at the saturation phase between 3-field and 6-field two-fluid models is 1.4%. Therefore, the 3-field two-fluid model is good enough to qualitatively understand the ELM thresholds due to P-B modes and quickly simulate early phase of ELM crashes with strongly unstable pedestals. However, ELM dynamics is a multi-scale problem, ranging from meso-scale MHD events to micro-scale turbulent dissipation due to electron gyro-radius effects. In order to simulate a ELM cycle and perform experimental validations, sophisticated multi-field models are also under development to obtain (1) ELM power loss via separate ion and electron channels, (2) ELM power depositions on plasma facing components (PFCs), and (3) self-consistent turbulence and transport between ELMs for the pedestal profiles rebuild. Furthermore, we find that the parallel thermal diffusivities are large on the top of pedestal plasmas, which prevent the further encroachment of ELM perturbation into core plasmas and therefore leads to steady state L-mode profiles. This motivates us to develop a nonlocal parallel Gyro-Landau-fluid thermal transport model valid in all collisionality regimes.

Both two-fluid and gyro-fluid simulation results show that for a density or temperature scan with a fixed pressure profile and for a ballooning-dominated equilibrium, the FLR effect can significantly decrease the ELM size because high- $n$  modes are stabilized. For typical experimental scenarios with natural transition between peeling dominated and ballooning dominated equilibria, the scaling characteristics of the ELMs size will be given in a future publication.

Finally, we have developed non-Fourier, configuration-space-based approaches for the computation of Landau-fluid

operators. We find that the fast non-Fourier approach has a computational cost scaling for large numbers of grid cells similar to the Fourier approach. The advanced gyro-fluid models with closure of high moments are under active development to simulate the meso-scale ELM dynamics and micro-scale turbulence valid in all collisionality regimes, which preserve particle, momentum and energy conservation, and include Landau damping, linear and nonlinear FLR, toroidal drifts, and drift resonance.

## ACKNOWLEDGMENTS

The authors wish to acknowledge W. Dorland, M. E. Fenstermacher, G. W. Hammett, A. W. Leonard, W. M. Nevins, F. L. Waelbroeck, and H. R. Wilson for useful discussions. This work was performed for USDOE by LLNL under DE-AC52-07NA27344, LLNL LDRD project 12-ERD-022, and LDRD project 11-ERD-058, the China Scholarship Committee under Contract No. 2011601099, and the China Natural Science Foundation under Contract No.10721505, LLNL-JRNL-605975.

<sup>1</sup>B. D.udson, M. V. Umansky, X. Q. Xu, P. B. Snyder, and H. R. Wilson, *Comput. Phys. Commun.* **180**, 1467 (2009).

<sup>2</sup>P. B. Snyder and G. W. Hammett, *Phys. Plasmas* **8**, 3199 (2001).

<sup>3</sup>D. H. E. Dubin, J. A. Krommes, C. Oberman, and W. W. Lee, *Phys. Fluids* **26**, 3524 (1983).

<sup>4</sup>X. Q. Xu, B. D.udson, P. B. Snyder, M. V. Umansky, and H. Wilson, *Phys. Rev. Lett.* **105**, 175005 (2010).

<sup>5</sup>D. Biskamp, *Magnetic Reconnection in Plasmas* (Cambridge University Press, Cambridge, 2000), p. 204.

<sup>6</sup>F. I. Parra and P. J. Catto, *Plasma Phys. Controlled Fusion* **51**, 095008 (2009).

<sup>7</sup>X. Q. Xu, R. H. Cohen, T. D. Rognien *et al.*, *Phys. Plasma* **7**, 1951 (2000).

<sup>8</sup>B. J. Burke, S. E. Kruger, C. C. Hegna, P. Zhu, and P. B. Snyder, *Phys. Plasmas* **17**, 032103 (2010).

<sup>9</sup>X. Q. Xu, B. D.udson, P. B. Snyder, M. V. Umansky, H. R. Wilson and T. Casper, *Nucl. Fusion* **51**, 103040 (2011).

<sup>10</sup>P. W. Xi, X. Q. Xu, X. G. Wang, and T. Y. Xia, *Phys. Plasmas* **19**, 092503 (2012).

<sup>11</sup>T. Y. Xia, X. Q. Xu, B. D.udson, and J. Li, “Nonlinear simulations of peeling-ballooning modes with parallel velocity perturbation,” *Contrib. Plasma Phys.* **52**(5-6), 353–359 (2012).

<sup>12</sup>T. Y. Xia, X. Q. Xu, Z. X. Liu, S. C. Liu, B. Gui, and J. G. Li, in *24th IAEA Fusion Energy Conference, San Diego, California* (2012), Paper TH/5-2Ra.

<sup>13</sup>T. Y. Xia and X. Q. Xu, “Five-field simulations of peeling-ballooning modes using BOUT++ code,” *Phys. Plasmas* **20**, 052102 (2013).

<sup>14</sup>T. Y. Xia, X. Q. Xu, and P. W. Xi, “Six-field two-fluid simulations of peeling-ballooning modes using BOUT++,” *Nucl. Fusion* (to be published).

<sup>15</sup>P. C. Stangeby, *The Plasma Boundary of Magnetic Fusion Devices* (Taylor & Francis, New York, 2000), p. 660.

<sup>16</sup>P. W. Fundamenski, *Plasma Phys. Controlled Fusion* **47**, R163 (2005).

<sup>17</sup>A. Loarte, G. Saibene, R. Sartori, D. Campbell, M. Becoulet, L. Horton, T. Eich, A. Herrmann, G. Matthews, N. Asakura, A. Chanin, A. Leonard, G. Porter, G. Federici, G. Janeschitz, M. Shimada, and M. Sugihara, *Plasma Phys. Controlled Fusion* **45**, 1549 (2003).

<sup>18</sup>A. W. Leonard, N. Asakura, J. A. Boedo *et al.*, *Plasma Phys. Controlled Fusion* **48**, A149–A162 (2006).

<sup>19</sup>G. W. Hammett and F. W. Perkins, *Phys. Rev. Lett.* **64**, 3019 (1990).

<sup>20</sup>M. A. Beer and G. W. Hammett, *Phys. Plasmas* **3**, 4046 (1996).

<sup>21</sup>A. M. Dimits, I. Joseph, M. V. Umansky, P. W. Xi, and X. Q. Xu, “Efficient non-Fourier implementation of Landau-fluid operators in the BOUT++ code,” *Bull. Am. Phys. Soc.* **57**, 143 (2012).

<sup>22</sup>M. Ottaviani and G. Manfredi, *Phys. Plasmas* **6**, 3267 (1999).

<sup>23</sup>A. M. Dimits, G. Bateman, M. A. Beer, B. I. Cohen, W. Dorland, G. W. Hammett, C. Kim, J. E. Kinsey, M. Kotschenreuther, A. H. Kritz, L. L. Lao, J. Mandrekas, W. M. Nevins, S. E. Parker, A. J. Redd, D. E. Shumaker, R. Sydora, and J. Weiland, *Phys. Plasmas* **7**, 969 (2000).